

See discussions, stats, and author profiles for this publication at: <https://www.researchgate.net/publication/231232797>

Nucleation and Growth Kinetics of (R)-Mandelic Acid from Aqueous Solution in the Presence of the Opposite Enantiomer

ARTICLE in CRYSTAL GROWTH & DESIGN · JUNE 2010

Impact Factor: 4.89 · DOI: 10.1021/cg900661z

CITATIONS

6

READS

23

4 AUTHORS:



Yan Zhang

Memorial University of Newfoundland

27 PUBLICATIONS 221 CITATIONS

[SEE PROFILE](#)



Shimin Mao

The University of Western Ontario

6 PUBLICATIONS 19 CITATIONS

[SEE PROFILE](#)



Ajay Ray

The University of Western Ontario

175 PUBLICATIONS 4,983 CITATIONS

[SEE PROFILE](#)



Sohrab Rohani

The University of Western Ontario

280 PUBLICATIONS 3,342 CITATIONS

[SEE PROFILE](#)

Nucleation and Growth Kinetics of (*R*)-Mandelic Acid from Aqueous Solution in the Presence of the Opposite Enantiomer

Yan Zhang, Shimin Mao, Ajay K. Ray, and Sohrab Rohani*

Department of Chemical and Biochemical Engineering, The University of Western Ontario, London, Ontario, N6A 5B9, Canada

Received June 12, 2009; Revised Manuscript Received May 13, 2010

ABSTRACT: Resolution of mandelic acid (MA), a racemic compound, is presented in this article using direct crystallization from enantiomeric enriched water solutions. Final crystals with enantiomeric excess (*ee*) of (*R*)-MA higher than 96.4% were obtained. Because of the presence of the opposite enantiomer ((*S*)-MA), it was reported that nucleation and growth of (*R*)-MA was inhibited at the initial stage of the experiment (Perlberg, et al. *Ind. Eng. Chem. Res.* **2005**, *44*, 1012–1020). In order to understand the nucleation and growth kinetics of (*R*)-MA in the presence of (*S*)-MA, batch crystallization experiments were performed for controlled linear cooling mode with various operating conditions. Nucleation and growth parameters were then estimated by nonlinear fitting the measured liquid concentrations obtained from the signals of in situ attenuated total reflectance infrared (ATR-IR) spectroscopy and online polarimetry with model predictions. The effects of supersaturation, seed amount, cooling rate, and the presence of opposite enantiomer on the growth and nucleation rate of (*R*)-MA were discussed.

1. Introduction

Separation of synthetically produced racemates still dominates as the most used approach for obtaining an enantiomerically pure product in the pharmaceutical industry. Such separations are most often performed by formation and crystallization of diastereomeric derivatives and by chromatography, although direct crystallization methods could be cheaper and simpler.¹ Direct crystallization relies on the principle of seeding a supersaturated racemic solution with the desired enantiomer. Such methods, however, can only be applied to racemic conglomerates, which is estimated to be only 5–10% of all organic racemates.² Recently, the applicability of direct crystallization was extended to racemic compound forming systems by combining with some pre-enantiomeric enrichment processes such as preparative chromatography.^{3,4} Though theoretically feasible, research on implementation of direct crystallization to racemic compounds is seldom reported. The major challenge for implementation of direct crystallization to racemic compounds lies in the complicated influence of the opposite enantiomer on both the thermodynamic and kinetic features of the process. Research from both experimental and theoretical aspects is needed for such an application, which is the focus of this work.

Reliable kinetic data are of great importance for the modeling, control, and operation of the crystallization process.^{5–7} However, despite the fundamental importance of direct crystallization in the effective optical resolution of racemates, kinetic studies performed in suspension crystallizers are still scarce.⁸ In the study of the crystallization from enantiomeric-enriched mandelic acid solutions,^{9,10} the presence of the opposite enantiomer is known to significantly decrease the growth rate of the desired enantiomer. However, the reason for such an inhibition effect was not given in these studies.^{9,10} Later, Angelov and co-workers published more details on acquiring the nucleation and growth kinetics of L- and D-threonine, a

conglomerate forming system, in their study of the optimal operation of enantioseparation by batch-wise preferential crystallization.¹¹ Because of the thermodynamic complexity of the compound forming system, it is hard to find the kinetics of compound forming systems by direct crystallization. This study aims to investigate how the two enantiomers of a compound forming system interact in a solution upon crystallization and how the nucleation and growth kinetics of the desired enantiomer is affected by the presence of the opposite enantiomer.

Mandelic acid was chosen as a model material because it is commonly used as a resolving agent for chiral separation, and consequently much of the thermodynamic data we need are already available.^{12,13} Several seeded cooling crystallization batches were conducted at various operating conditions to derive the kinetic parameters. With the help of online monitoring technology, that is, in situ attenuated total reflectance Fourier transform infrared (ATR-FTIR) spectroscopy and online polarimetry, the concentration profiles of the two enantiomers in the mother liquor were recorded. By fitting the experimental concentration and the batch mean particle size data with model calculations, kinetic parameters for the nucleation and crystal growth of (*R*)-mandelic acid (MA) were obtained. The influence of the operating variables such as initial *ee* of the solution, supersaturation, and cooling rate on the crystal growth rate and nucleation rate was studied. The results of the present work provide useful and essential information in controlling the crystallization process for the desired enantiomer separation with high purity.

2. Materials and Methods

2.1. Materials. Enantiopure (*R*)-mandelic acid (99%) and (*S*)-mandelic acid (>99%) as well as the racemate, (*R,S*)-mandelic acid (99%), were purchased from Alfa Aesar (Heysham, Lancashire, UK) and used without further purification. Ultrapure water, prepared from the Milli-Q Integral 5 system (Millipore, Billerica, MA, US) was used as the solvent of the crystallization process. HPLC grade isopropyl alcohol and hexane were purchased from EMD Chemicals (Gibbstown, NJ, US).

*Corresponding author. E-mail: srohani@uwo.ca.

Seed crystals of pure (*R*)-MA ranged from 212 to 300 μm were prepared using a GA-6 Gilsonic Autosiever (Gilson, Worthington, OH). To avoid dissolving in the solution, seed crystals were added from a head nozzle to the crystallizer at the 2 $^{\circ}\text{C}$ below the starting temperature of each crystallization batch. A M400LF focused beam reflectance (FBRM) system (Lasentec, Redmond, WA, US) was used to determine the seeding effect.

2.2. Batch Crystallization. The crystallization experiments were performed in a jacketed 250 mL glass crystallizer. A Teflon-coated stirrer bar was used for magnetic stirring ($25 \times 8 \text{ mm}$), which was kept at a constant stirring rate of 300 rpm to ensure that the crystals were well distributed in the solution. The temperature in the crystallizer was controlled by a Julabo FP50 bath circulator (Allentown, PA, US). The FBRM system was used to monitor the nucleation of fresh nuclei or the dissolution of the solids in the solution. An in situ ATR-FTIR (Hamilton Sundstrand, CA) was used for collecting of infrared spectra. The IR spectra were related to the total solute concentration in the solution using a calibration curve. The optical rotation of the solution which indicates the concentration difference of the two enantiomers was measured continuously by an Autopol IV polarimeter (Rudolph Research Analytical, Hackettstown, NJ, US). Crystal-free solution with a volume of 20 mL was drawn from the crystallizer every 4 min using a DOSE IT P910 peristaltic pump (IBS Biosciences, Switzerland) with the help of a membrane filter and heated during the transport to an online polarimeter. After measurement, the solution was pumped back into the crystallizer. Signals from ATR-FTIR and polarimeter were then converted to obtain the individual concentration of each enantiomer in the solution.

A typical experimental run was performed as follows. The aqueous solution with different initial *ee* of (*R*)-MA for the batch crystallization was prepared according to the solubility determined from the experiment. The prepared solution was heated up and maintained 30 min at the starting temperature to ensure that all of the crystals were dissolved. The temperature of the solution was then quickly lowered by 2 $^{\circ}\text{C}$, and at this temperature, a predetermined amount of homochiral seed crystals of (*R*)-MA were added to initiate the experiment. The solution, being stirred at a rate of 300 rpm, was then linearly cooled to the ending temperature at a rate of 0.02 $^{\circ}\text{C}/\text{min}$ and maintained at that temperature for 20 min. At the end of each experiment, the slurry was quickly filtered through a 1 μm filter paper under reduced pressure. Subsequently, crystals were air-dried at 60 $^{\circ}\text{C}$ overnight and the size distribution was measured. The experimental conditions for the crystallization batches are summarized in Table 2. Run 2 and Run 3 were replicated and the repeatability of the batch crystallization processes was found to be very good.

2.3. Analytical Methods. An Agilent 1200 series HPLC system (Agilent Technologies, Palo Alto, CA) with ChiralCel OD-H column (Chiral Technologies, West Chester, PA) was used to measure the optical purity of final products. The mobile phase was a mixture of hexane and isopropyl alcohol (85:15, v/v), with 0.1% of acetic acid used as a modifier. HPLC analyses were performed at 25 ± 0.1 $^{\circ}\text{C}$ with an elution flow rate of 0.7 mL/min. The detection wavelength was 254 nm.

The optical purity of final products was also verified using a Mettler Toledo 822e DSC system, together with the STARe software. Final products were examined by differential scanning calorimetry (DSC) from 25 to 150 $^{\circ}\text{C}$ at a heating rate of 5 $^{\circ}\text{C}/\text{min}$.

The powder X-ray diffraction (XRD) patterns of the final products were also tested using a Rigaku-MiniFlex powder diffractometer and were compared with those of enantiomeric pure (*R*)-MA and (*R,S*)-MA. Samples were scanned from a diffraction angle (2θ) of 5 $^{\circ}$ to 55 $^{\circ}$ with a step size of 0.05 $^{\circ}$ and a counting time of 1 s for each step. The crystal size distribution of the final product was measured using a Malvern Mastersizer (Malvern Instruments, UK) with a Sirocco 2000 sample handling unit.

3. Theoretical Aspects

3.1. Direct Crystallization from Enantiomeric Enriched Solution. For racemic compound forming systems, crystallization alone is not capable of obtaining pure enantiomers

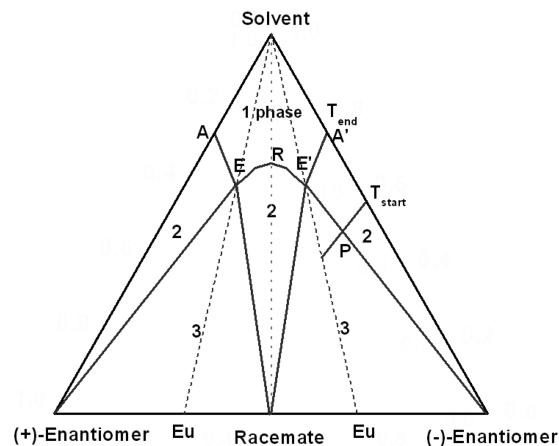


Figure 1. Illustration of a typical ternary phase diagram for a racemic compound forming system.

from the racemic mixtures; pure enantiomer can only be produced by direct crystallization when the solution composition exceeds the eutectic composition of the system.^{3,14} The principle of direct crystallization process for resolution of a racemic compound can be illustrated in a typical ternary solubility phase diagram as shown in Figure 1. The vertexes of the triangle represent the pure components: the solvent (on top), the (+)- and (−)-enantiomers (left and right). The area within the triangle can then be divided into a number of domains.¹⁵ Mixtures in the upper region comprise single phase solutions. On reducing the water content, a number of regions emerge in which solids and solutions are in equilibrium. The regions on the left- and right-hand sides are the two-phase areas in which crystals of pure enantiomers are in equilibrium with saturated solutions having compositions on lines AE or A'E'. In the middle two-phase region, the racemic compound is in equilibrium with solutions of compositions on line ERE'. The remaining regions are the three-phase areas in which mixtures of pure enantiomers and racemic compound crystals are in equilibrium with solutions of fixed composition. It follows that crystallization in two-phase regions would only yield one solid form, that is, pure enantiomer or racemic crystals, respectively, while crystallization in the three-phase region will yield products that are mixtures of pure enantiomer and the racemic compound crystals. Hence, pure enantiomers can be obtained by direct crystallization when the process is controlled within the left- or right-hand side of the two-phase regions.

In order to obtain pure enantiomers, the starting composition of the enantiomeric enriched solution should be selected based on the temperature difference ($T_{\text{start}} - T_{\text{end}}$) and the eutectic composition at the ending temperature in case of cooling crystallization. On the basis of the solubility data, the starting and the ending temperatures of a batch crystallization process were first determined. The eutectic point E' of the ending temperature (T_{end}) was then fixed on the ternary phase diagram. Connecting the point corresponding to pure enantiomer to point E' gives a line which intersects the solubility curve of the starting temperature (T_{start}) at point P. The composition of point P corresponds to the lowest initial enantiomeric excess value (ee_0) of the desired enantiomer.

3.2. Modeling and Simulation. A simplified dynamic model for an ideally mixed batch crystallizer was used assuming no crystal agglomeration, abrasion, and breakage.^{16–18} It was

assumed that there was no interdependence of the growth rate of each enantiomers and crystal growth rate was size-independent. Since the solubility of (*R,S*)-MA is much higher than that of pure enantiomer and the solution contains only about 20% (*S*)-MA, supersaturation of (*R,S*)-MA and (*S*)-MA could not be achieved during the crystallization process. Therefore, only crystallization of (*R*)-MA was considered. The population balance and solute balance of (*R*)-MA in a seeded batch crystallizer are as follows:

$$\frac{\partial n(L, t)}{\partial t} + \frac{G(t) \partial n(L, t)}{\partial L} = 0 \quad (1)$$

$$\frac{dc_R}{dt} = -3\rho_c k_v G(t) \int_0^{L_{\max}} n(L, t) L^2 dL \quad (2)$$

where $n(L, t)$ denotes the population density for (*R*)-MA crystals; G is crystal growth rate; t and L are the time and crystal size coordinates; c_R is the concentration of (*R*)-MA in the solution; ρ_c is the crystal density; k_v is the volume shape factor.

Seed crystals were used for all the batches and the population density of seed crystals at time zero was assumed to be a parabolic distribution with the coefficient (a_0) determined by mass balance. The values of a_0 for different experimental runs are listed in Table 1. The initial and boundary conditions for eqs 1 and 2 can be described by

$$n(L, 0) = \begin{cases} a_0(300 - L_s)(L_s - 212) & \text{with } 212 < L_s < 300 \mu\text{m} \\ 0 & \text{otherwise} \end{cases} \quad (3)$$

$$c_R(t = 0) = c_{R,0} \quad (4)$$

$$n(0, t) = \frac{B(t)}{G(t)}|_{L=0} = 0 \quad (5)$$

Because seed crystals are already dispersed in the crystallizing medium, secondary nucleation can occur at supersaturation levels which are significantly lower than those at which primary nucleation takes place.¹⁹ Nucleation and growth rate models of (*R*)-MA from the aqueous solution in the presence of (*S*)-MA can be describes by

$$B = k_{b0} \exp(-E_b/RT) \Delta c_R^b M_T \quad (6)$$

$$G = k_{g0} \exp(-E_g/RT) \Delta c_R^g \quad (7)$$

where k_{b0} and k_{g0} are the rate coefficients; E_b and E_g are the activation energies of birth and growth; R is the universal gas constant; T is the temperature; and M_T is the suspension density. It should be stressed that the supersaturation of (*R*)-MA (Δc_R) defined here is different from the ordinary case. It is known that the presence of the opposite enantiomer will change the total solute concentration in equilibrium; therefore, Δc_R (g/g water) in the solution with the presence of opposite enantiomer should be the difference between the concentration of (*R*)-MA and the equilibrium mass fraction of (*R*)-MA in the mixture solution, expressed as, $\Delta c_R = c_R - x_R c_{sol}^{eq}$, c_{sol}^{eq} is the solubility of the mixture solution, changing with both temperature and *ee* value of the solutions, x_R is the mass fraction of (*R*)-MA, $x_R = c_R/(c_R + c_S)$.

Method of lines was used in this work to obtain the crystal particle size distribution and concentration profile of mother liquor by solving eqs 1–7 simultaneously. The partial differential

Table 1. Solubility of Mandelic Acid Water Solutions at Different Temperatures

$T, ^\circ\text{C}$	solubility with different <i>ee</i> values, g/g water				
	1.0	0.8	0.6	0.5	0.38 ^a
5	0.062				0.102
10	0.071		0.095		0.121
15	0.083			0.123	0.153
15.65			0.114		
16.2		0.093			
20	0.094		0.139	0.153	0.187
20.32		0.113			
25	0.103		0.171	0.194	0.285
26.0		0.143			
28.3			0.209		
30	0.125				
solubility constants					
	0.8 < <i>ee</i> ≤ 1.0	0.6 < <i>ee</i> ≤ 0.8	0.5 < <i>ee</i> ≤ 0.6	0.38 < <i>ee</i> ≤ 0.5	
A0	5.45×10^{-2}	6.03×10^{-2}	7.53×10^{-2}	8.5×10^{-2}	
A1	1.38×10^{-3}	3.28×10^{-4}	-3.85×10^{-4}	3.6×10^{-3}	
A2	3.1×10^{-5}	1.11×10^{-4}	1.76×10^{-4}	-2.75×10^{-4}	
A3	0	0	0	1.3×10^{-5}	
B0	5.98×10^{-2}	0.127	0.186	0.161	
B1	-9.94×10^{-3}	-8.48×10^{-4}	4.87×10^{-2}	0.183	
B2	7.71×10^{-4}	3.65×10^{-4}	-6.3×10^{-3}	-2.04×10^{-2}	
B3	0	0	2.06×10^{-4}	6.21×10^{-4}	
C	1.0	0.8	0.6	0.5	

^a Solubility data for solutions with *ee* equal to 0.38 are based on the experimental results reported by Lorenz et al.¹²

equation (PDE) was discretized in space by means of a finite difference approximation and converted into a set of initial value problems (IVPs) of ordinary differential equations (ODEs). The resultant stiff ODEs of the initial value problems were then solved using the subroutine DIVPAG in IMSL.

3.3. Parameter Estimation. Optimization provides an important approach to parameter estimation for nonlinear batch systems. In this study, nondominated sorting genetic algorithm (NSGA), an evolutionary optimization approach, was applied to determine the nucleation and growth kinetic parameters of (*R*)-MA from aqueous solution in the presence of the opposite enantiomer. NSGA was used to generate random guesses of the kinetic parameters, with these random generated kinetic parameters, the dynamic model equations (eqs 1–7) were solved and the resulting predictions of the solution concentrations were obtained. The kinetic parameters were determined by tuning the model predicted concentrations to the experimental data using NSGA so that the objective function, that is, the minimum sum of squares error between experimental measurements and model predictions could be achieved. The optimization formulation can be described as follows:

$$\text{minimize } F = \sum_{j=1}^n (c_{R,j}^c - c_{R,j}^m)^2$$

$$\text{subject to } 0.9L_{43}^m < L_{43}^c < 1.1L_{43}^m$$

$$\text{with } c_{R,j}^c = \phi_1(k_{b0}, E_b, b, k_{g0}, E_g, g)$$

$$L_{43}^c = \phi_2(k_{b0}, E_b, b, k_{g0}, E_g, g)$$

where $c_{R,j}^m$ and $c_{R,j}^c$ are the measured and the calculated concentrations of (*R*)-MA at each sampling point j . L_{43}^m and L_{43}^c are the measured and the calculated volume-weighted mean size of the final product.

As the dimensionality of the search space for the above optimization problem is very high, it is difficult for deterministic algorithms to find the final optimal solutions. NSGA-II,²⁰ an elitist NSGA using an elite-preservation strategy as well as an explicit diversity-preserving mechanism, and its jumping genes (JG) adaptation were chosen in this study for the least-squares fitting. Elitism of NSGA-II helps the solution to converge near the true global optimum but results in decreased genetic diversity. The JG operator helps improve the diversity of the gene pool and, thus, counteracts the negative effect of elitism. NSGA-II-JG has been applied to various optimization problems and proven to be capable of providing the global optimal solutions with reduced computation time.^{21,22} Details of this algorithm can be found elsewhere.²³

4. Results and Discussion

4.1. Determination of Liquid Concentration and Solubility of Enantiomeric Enriched Solution. The calibration model of the IR spectra of mandelic acid in water is generated based on spectra in the range 900–1700 cm^{-1} collected from a series of undersaturated solutions with known solute concentrations. The quantification of the IR spectra for mandelic acid was based on the analysis of the heights of three different peaks at 1068.4, 1135.9, and 1191.8 cm^{-1} . The calibration curve was obtained by correlating the heights of the peaks (P) to the mandelic acid solutions with known concentrations. The calibration equation used to predict the total concentration of mandelic acid solution, in g/g water, is as follows:

$$c_R + c_S = 4.17 \times (P_{1068.4} - P_{1135.9}) - 2.04 \times (P_{1191.8} - P_{1135.9}) \quad (8)$$

This calibration model was then used to obtain the total solute concentration of mother liquor during the crystallization process from the in-line spectra gathered by the immersion probe. Figure 2a illustrates the in-line IR spectra of mandelic acid water solution for Run 3.

Quantitative determination of the total concentration for a cooling crystallization batch by IR spectroscopy is however not simple, although the applications are increasing in number.^{24,25} It was observed in our experiments that measurements become less accurate indicated by the drift in the spectra after a large amount of fresh nuclei are generated by secondary nucleation. This suggests that, as long as no small crystals exist in the slurry, the mother liquor concentration can be quite accurately monitored in situ during a seeded crystallization. This observation coincides with those reported previously.²⁵ And, this is also the reason why our operating conditions were selected to avoid the generation of a large amount fine crystals by secondary nucleation.

Online polarimeter was used in this study to record the concentration difference of the two enantiomers. The calibration curve of the polarimeter is illustrated in Figure 2b. The concentration difference of the two enantiomers, in g/g water, can be expressed as

$$c_R - c_S = 10^{-3} \times (0.017a_{589}^3 + 0.55a_{589}^2 - 3.1a_{589}) \quad (9)$$

where a_{589} (arc degree) is the optical rotation of the solutions at the wavelength of 589 nm. The online signal of the polarimeter at every sampling point for Run 3 is also indicated in Figure 2b. Signals from online polarimeter were proven to be quite consistent and reliable through our experimental

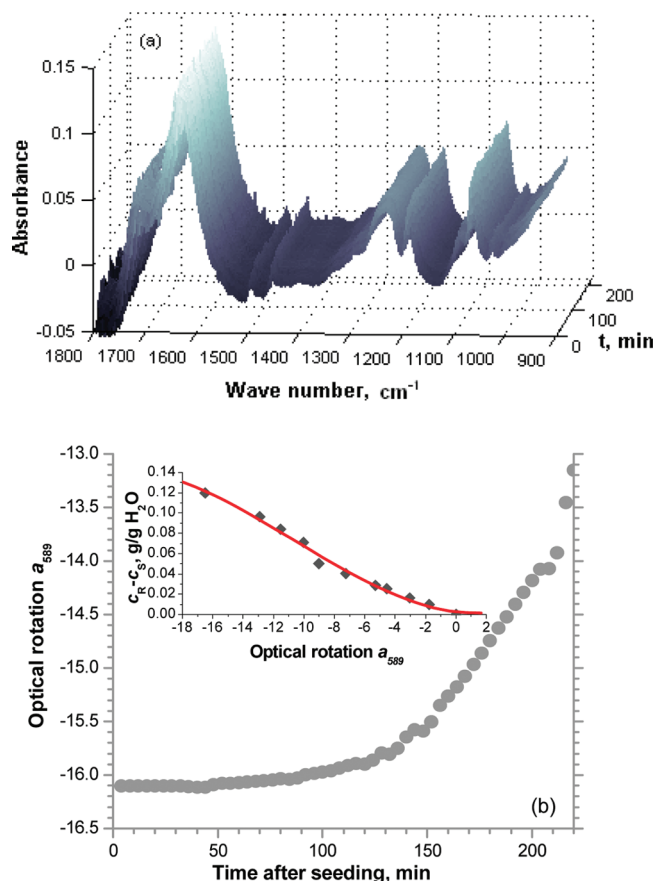


Figure 2. Experimental results of Run 3 from (a) in situ ATR-FTIR and (b) online polarimeter.

investigation. With the signals from both ATR-FTIR and online polarimeter, the individual concentration of (*R*)- and (*S*)-MA in the water solution could be determined.

Measurement of the solubility of enantiomeric enriched solutions is important since the solubility varies with both temperature and compositions of the solutions. The gravimetric method was used to measure the solubility of the enantiomeric enriched solutions at different temperatures and compositions. Table 1 lists the measured solubility of MA water solutions with different *ee* and temperatures. Solubility equations of the enantiomeric enriched solutions in g/g water, with *ee* between 0.38 to 1.0 and *T* within 15–30 °C, can be empirically expressed as

$$c_{\text{sol}}^{\text{eq}} = \sum_{i=0}^3 A_i T^i + 0.5(C - ee) \sum_{i=0}^3 B_i T^i \quad (10)$$

where *ee* is defined as $(c_R - c_S)/(c_R + c_S)$, the constants in the above equation are given in Table 1.

4.2. Kinetic Parameters. Operating conditions of the batch crystallization processes for the resolution of (*R*)-MA from enantiomeric enriched solution are illustrated in Table 2. Experimental data from Runs 2–4 were used to derive the crystallization kinetic parameters of (*R*)-MA in the presence of the opposite enantiomer. Runs 2–4 generated more than 160 concentration data points which are enough to derive the kinetic parameters by dynamic fitting. In order to narrow down the searching dimensions for the optimization, the values for kinetic order of nucleation and growth (*b* and *g*) were fixed at 1.5 and 1.0, respectively. Since fast nucleation is undesirable, kinetic order of nucleation, *b*, with the value of

Table 2. Operating Parameters of Direct Crystallization Processes for the Resolution of (*R*)-MA from Enantiomeric Enriched Solutions

parameter	symbol	Run 1	Run 2	Run 3	Run 4	Run 5	Run 6	unit
starting temperature	T_{start}	25	25	28	25	25	28	°C
seeding temperature	T_{seed}	23	23	26	23	23	26	°C
ending temperature	T_{end}	19	19	22	19	19	15	°C
cooling rate after seeding	r_c	0.02	0.02	0.02	0.02	0.02	0.05	°C/min
mass of solvent	W_{sol}	150	200	150	150	150	150	g
initial total concentration ^a	C_0	0.104	0.168	0.209	0.194	0.167	0.201	g/g H ₂ O
initial enantiomeric excess ^b	ee_0	100	64	60	50	64	60	%
seed amount	W_{seed}	0.31	0.34	0.31	0.34	1.36	0.27	g
coefficient for seeding $\times 10^3$	$a_0 \times 10^3$	6.6	5.38	6.6	7.2	28.9	5.74	(-)
enantiomeric excess of seed crystals	ee_s	100	100	100	100	100	100	%
crystal density of (<i>R</i>)-MA	ρ_c	1349						kg/m ³
shape factor of crystals	k_v	0.12						(-)

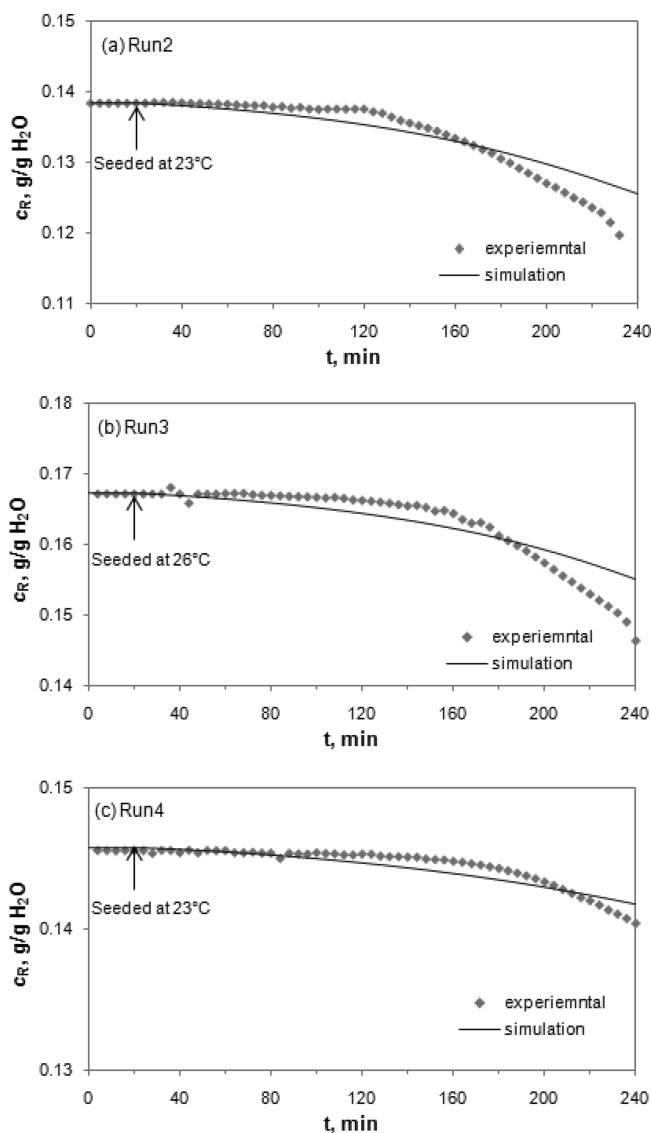
^aInitial total concentration of solute includes the concentrations of both (*R*)-MA and (*S*)-MA in water. ^bInitial enantiomeric excess refers to the enantiomeric excess of (*R*)-MA.

Table 3. Estimated Nucleation and Growth Kinetic Parameters for (*R*)-MA from Aqueous Solution

kinetic parameters					
		Run 1	Run 2–Run 4	Run 6	
rate		(Pure (R)-MA)			unit
nucleation	$k_{b0} \times 10^{-12}$	2.4	2.6 ± 0.2	2.4	(#/min)
	E_b	36.0	35.8 ± 0.2	36.6	kJ/mol
	b	1.5	1.5	1.5	(–)
growth	$k_{g0} \times 10^{-6}$	6.0	6.0 ± 1.5	12.0	($\mu\text{m}/\text{min}$)
	E_g	27.4	29.6 ± 0.6	28.7	kJ/mol
	g	1.0	1.0	1.0	(–)

1.5 seems reasonable. As for the value of g , it was reported²⁸ that growth kinetics for most of the stereoisomer resolution process has been essentially first-order with respect to supersaturation; therefore, the value of g was also set as 1.0 in this study. On the basis of the predetermined values of b and g , values of other kinetic parameters were then determined by fitting the model predictions to the three concentration profiles of (*R*)-MA in the solutions. The estimated nucleation and growth kinetic parameters, as well as their confidence intervals, are listed in Table 3. Figure 3 shows the comparison between the calculated and measured concentration profiles of (*R*)-MA for these three runs. As seen from these figures, the magnitudes of the values for the predicted concentration profiles are in good agreement with those obtained experimentally. The average deviations between the predicted and measured concentrations of (*R*)-MA for Runs 2–4 are 0.15, 0.17, and 0.06 g/100 g of solvent, respectively. The dynamic model with the estimated kinetic parameters could also predict the yield of (*R*)-MA crystals with errors of 8.49%, 12.36%, and 5.5% for Runs 2–4, respectively. However, notable deviations between the model predicted and experimentally obtained concentration profiles for the three runs still can be seen from Figure 3. Two major causes lead to such kinds of deviations. First is the measurement error. As discussed earlier, IR signals are not very accurate after secondary nucleation occurs. Therefore, experimental errors do exist in the measured concentration profile for (*R*)-MA. Another main cause is the solubility data used in the optimization program. Although we measured the solubility of the enantiomeric enriched water solutions with various temperature and ee values for MA, it is not possible for us to give the exact prediction of the solubility data for MA water solutions in the dynamic process.

The estimated kinetic parameters can be used to simulate the mass and particle size distribution (PSD) of the final crystals. The accuracy of the derived kinetic parameters

**Figure 3.** Measured and calculated concentration profiles of (*R*)-MA at different operating conditions.

could be verified by comparing the model predicted PSDs with those obtained from experiments, as illustrated in Figure 4. As seen from the plot, although the simulated final PSD of Run 1 shows some deviations from the experimentally obtained PSD, the volume-weighted mean size (L_{43}) from simulation is quite close to the measured values. The

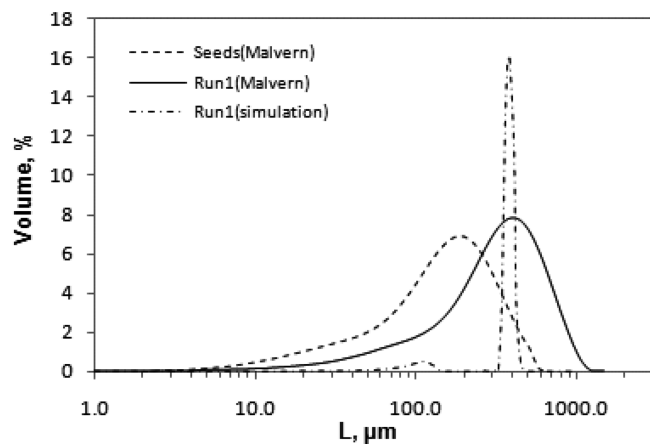


Figure 4. Measured and calculated PSDs of Run 1.

main causes of the discrepancy of the calculated and measured PSDs are 3-fold. First, crystals of (*R*)-MA have three dimensions, and it is not possible for the Mastersizer to obtain the measurement PSD data based on a single face of the crystals, while the predicted PSD is calculated based on only a single dimension of the crystals. Figure 4 illustrates the PSD of seed crystals with a size range of 212–300 μm . The measured PSD of seed crystals is much wider than the theoretical calculation. Second, in the mathematical model we neglected the breakage and agglomeration of the crystals. However, the breakage and agglomeration of crystals are unavoidable during the crystallization process. That is another reason why PSD from measurement is wider than that from simulation. In addition, the boundary condition used in the simulation seems too simplified which also leads to the deviation of the calculated PSD to the measured data. Since we forced the L_{43}^m value to be within the range of $\pm 10\%$ of L_{43}^m in the optimization program, kinetics parameters listed in Table 4 provided us the L_{43}^c values of 473.2 and 432.1 μm and for Runs 2 and 3 which are quite close to the L_{43}^m values listed in Table 3. With the constraints of L_{43} added in the optimization program, the estimated nucleation and growth kinetic parameters are reliable in predicting the real nucleation and growth rate of (*R*)-MA from aqueous solution. Population densities for Runs 2 and 3 which are used to calculate the L_{43}^c values are shown in Figure 5.

4.3. Influence of the Amount of Seed Crystals. Nucleation occurs at much lower supersaturation when crystals of the solute are already present or deliberately added.²⁶ It was observed that the secondary metastable zone width (MSZW) was much narrower than that of the primary nucleation metastable zone width.¹² The reduced MSZW is beneficial to the crystallization resolution of a compound forming system since the potential of nucleation of the racemic compound is significantly decreased.

However, the amount of seed can be critical in the control of the crystallization process for chiral separation.²⁷ The influence of the seed amount on the growth rates of (*R*)-MA in the presence (*S*)-MA was investigated by comparing the desupersaturation behavior as well as nucleation and growth rate of (*R*)-MA as a function of time for Run 2 and Run 5, in which small and large amounts of seed crystals were added respectively. From Figure 6a, it can be seen that the desupersaturation rate for Run 5 is much faster than that of Run 2 due to the large amount of seed crystals introduced. The use of increased seed amounts allows an increase in the rate of

Table 4. Crystal Properties Obtained from Crystallization Batches for the Resolution of (*R*)-MA from Enantiomeric Enriched Solutions

properties		Run 1	Run 2	Run 3	Run 4	Run 5	Run 6
yield ^a	%	4.29	8.5	11.28	2.51	13.43	31.5
ee ^b	%	100	98.2	97.6	99.1	100	96.4
L_{43}^m	μm	381.7	440.1	422.6	n.d. ^c	n.d.	708.1

^a Yield is defined as the ratio of product collected of (*R*)-MA to the amount of (*R*)-MA in the initial solution (amount of seed crystals has been excluded from the product). ^b Crops from Run 5 were washed using cold water; crops from Run 4 were washed with mixed solvent of hexane and isopropanol. Crops of all the other runs were analyzed without washing. ^c Not determined.

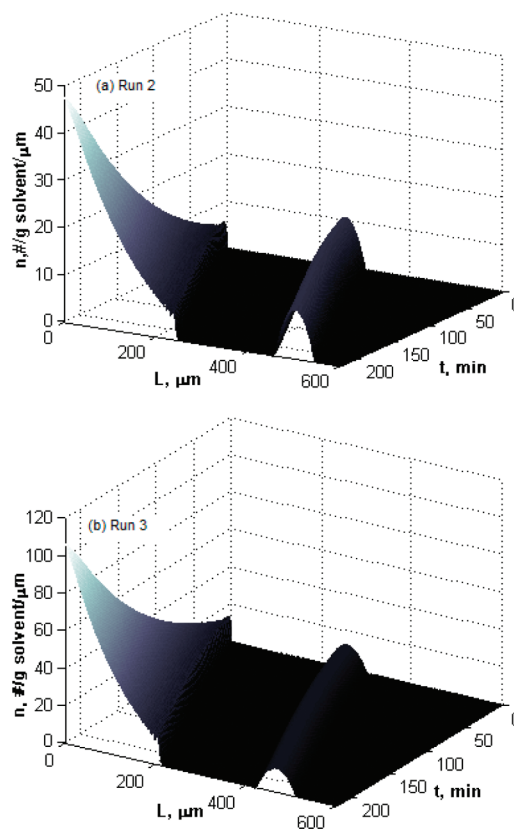


Figure 5. Predicted population density for (a) Run 2 and (b) Run 3.

desupersaturation by providing more surfaces for growth. In addition, large seeding amount helps to control the supersaturation. As a result, supersaturation of (*R*)-MA in Run 5 is much lower than that in Run 2.

Because of the relative lower supersaturation in Run 5, both nucleation and growth rates in Run 5 are lower than those in Run 2, as illustrated in Figure 6b. However, the reduction in nucleation rate is more pronounced. All these results indicate that a large seed amount is desirable in our application since it helps to prevent nucleation; therefore, the possibility for the nucleation of the racemic compound has also been greatly reduced.

4.4. Effect of Cooling Rate. The effect of cooling rates on crystallization kinetics has been studied widely. In this work, a fast cooling rate in Run 6 was observed to generate a fast growth rate of (*R*)-MA. Kinetics parameters which led to the best fitting of the experimental data of Run 6 are listed in Table 3. The effect was more pronounced on the growth rate constant, k_{go} . This is expected since the crystallizer is seeded and the crystal growth dominates the process. However, a

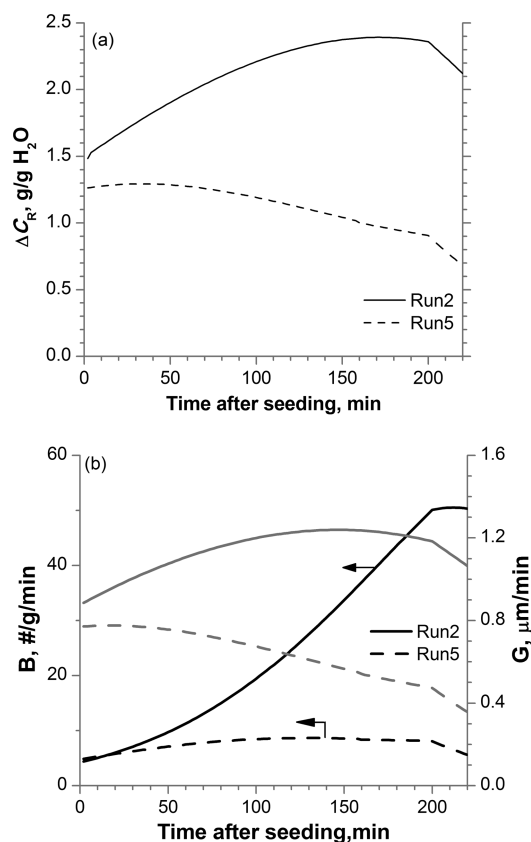


Figure 6. (a, b) Effect of seed amount on the nucleation and growth of (*R*)-MA from enantiomeric enriched water solutions.

fast cooling rate is not recommended in our application since the possibility for triggering the secondary nucleation of the undesired products will increase significantly in this case.

4.5. Influence of the Opposite Enantiomer. Study of the influence of the opposite enantiomer on the nucleation and growth of the desired enantiomer is important for understanding the kinetics for the direct crystallization process for both racemic conglomerate and compound forming systems. Because of the presence of the opposite enantiomer, both thermodynamic and kinetic features of the process are altered. In this study, crystallization of pure (*R*)-MA was performed under comparable operating conditions with a difference only in the initial *ee* values of the solutions to study the effect of the opposite enantiomer. Kinetic parameters derived from the crystallization process of pure (*R*)-MA (Run 1) were also listed in Table 3 for comparison. Except for E_g , all the other kinetic parameters converged to the very similar values. However, the best fitting value for E_g derived from Runs 2–4 is significantly higher than that obtained from Run 1. This may be because the suppressant (*S*)-MA poisons the growth surface; therefore, growth rate of (*R*)-MA tend to be integration controlled, leading to an increase of the activation energy of growth.²⁸

Figure 7 compares the transient supersaturation profiles and nucleation and growth rates for Run 1, Run 2, and Run 4. Because of the huge influence of the opposite enantiomer on the solubility equilibrium of the solution, distinct supersaturation profiles of (*R*)-MA were obtained over the same temperature range for these three runs. As seen from Figure 7a, Run 1 has the lowest magnitude of supersaturation, while supersaturation in Run 2 is the highest during the first 60 min of the process and finally it is exceeded by that in Run 4.

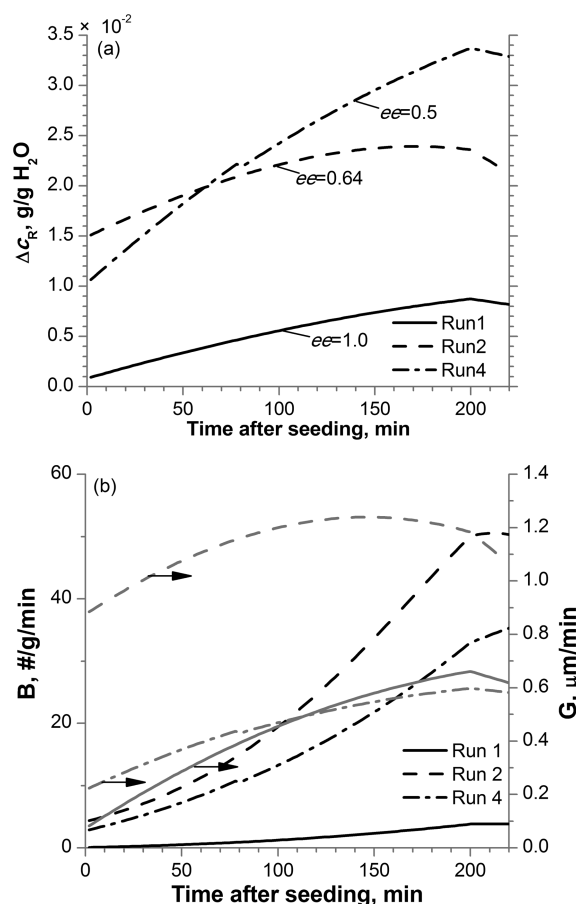


Figure 7. (a, b) Effect of the presence of (*S*)-MA on the nucleation and growth of (*R*)-MA from enantiomeric enriched water solutions.

Although supersaturation in Run 1 is much lower than that in Run 4, the growth rate of (*R*)-MA in Run 1 is even higher than that in Run 4 during the second half of the process, which suggests the inhibition of growth of (*R*)-MA due to the presence of (*S*)-MA.

For the crystallization of (*R*)-MA from the enantiomeric-enriched aqueous solution, the opposite enantiomer is always present as an impurity in the crystallization medium. The enantiomeric impurity was found to significantly affect the growth of the homochiral crystals.^{9,10} Crystal growth involves complex dynamical processes at the molecular level, and the task of modeling this phenomenon is certainly made more difficult with the addition of surface impurities. Hence, experimental observations were used as much as possible to the study the influence of the opposite enantiomer on the crystal growth and nucleation of (*R*)-MA in this work. It can be seen from Figure 7 that the inhibition effect increases with an increasing amount of the opposite enantiomer. The most probable mechanism for retardation of the crystallization growth could be the blocking of the crystal surface by the impurities. With the increasing concentration of the opposite enantiomer in the crystallization medium, more active sites on the crystal surface are embedded by the opposite enantiomer. And the release of such impurity molecules embedded on the surface results in a retardation of the crystal growth of (*R*)-MA. To understand the quantitative insight of the effect, further research work is needed.

The effect of (*S*)-MA on the crystal morphologies of final products are shown in the optical images illustrated in Figure 8. Large amounts of the rhombohedral-shaped plates and a small

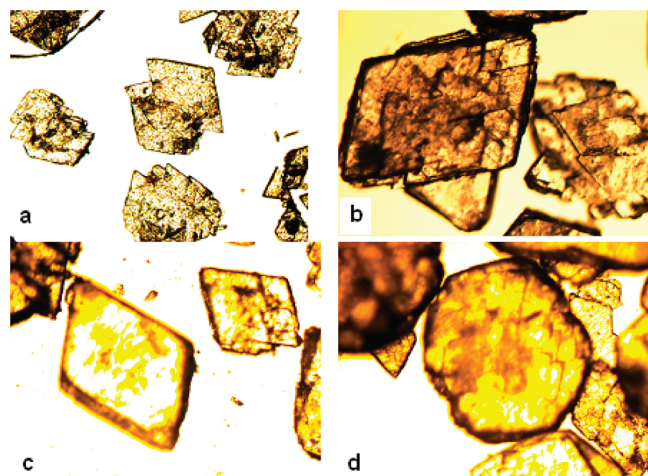


Figure 8. Microscopic images of the final crystal products obtained from (a) Run 1; (b) Run 2; (c) Run 3; and (d) Run 6.

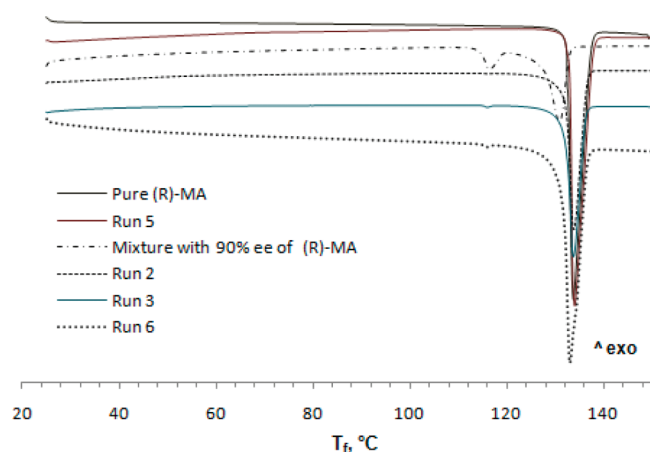


Figure 9. DSC thermograms of final crystal products.

amount of the hexagonal-shaped plates for the final products were obtained from the six crystallization batches. Both forms have been confirmed available by previous studies on the morphology of the pure enantiomer of MA.^{29,30} Therefore, the presence of the opposite enantiomer was not observed to affect the morphology of the homochiral crystals.

The presence of (*S*)-MA on the optical purity of final crystal products is of great importance when applying direct crystallization for chiral separation. Crystal properties obtained from the four crystallization batches are listed in Table 4. The optical purities of the final crystal products for Runs 2–6 were analyzed to examine the applicability of direct crystallization to compound forming systems. Results of HPLC analyses showed that crystals with an *ee* value of (*R*)-MA higher than 96% were achieved for all runs. The optical purity of the final crystal products was also verified by means of DSC measurements. The DSC thermograms of final crystal products as well as those of the pure (*R*)-MA and mixture with 90% *ee* of (*R*)-MA are shown in Figure 9. DSC results confirmed that products are of extremely higher optical purities, although tiny eutectic peaks are also observed showing the presence of a very small amount (<2%) of (*S*)-MA in the products. Since we did not wash the crops from Runs 2, 3 and 6, the presence of a small amount of (*S*)-MA in the final crystals of these batches may be the residual of the (*S*)-MA from the mother liquor. This is confirmed by

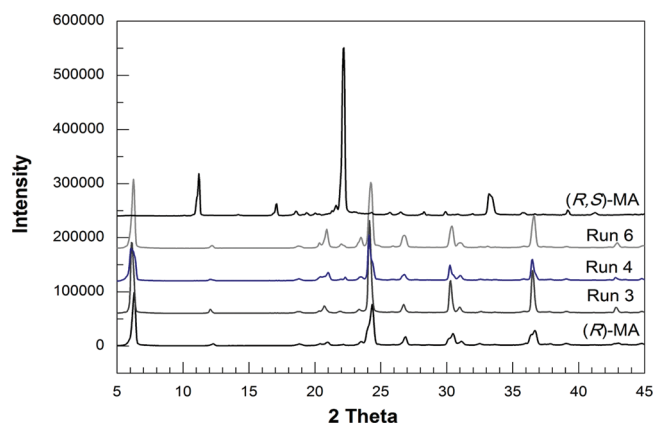


Figure 10. Powder XRD patterns of final crystal products.

the extremely high optical purity of the final products obtained from Run 4 and Run 5, for which crops from crystallization batches were washed by clean solvent.

The XRPD patterns of crystal products are also compared with those of pure (*R*)-MA and (*R,S*)-MA as shown in Figure 10. Although slight shifts probably caused by systematic distortions in some peaks could be observed, XRPD patterns of the products from Run 3, Run 4, and Run 6 are almost identical with that of pure (*R*)-MA (see for example the four largest peaks at 2θ angles of 6.2°, 24.2°, 30°, and 36.6°, respectively), which confirms the high purity of products obtained.

All these analytical results proved that resolution of MA from enantiomeric enriched solution can be achieved, and almost pure enantiomer could be obtained from the seeding cooling crystallization experiments within a certain safe supersaturation limit. In addition, the efficiency of such resolution processes is satisfactory since the yield of such processes (Run 2) may even exceed that obtained from recrystallization of pure enantiomer (Run 1) as shown in Table 4 under the same temperature range.

5. Conclusions

Resolution of MA by direct crystallization and kinetic study of (*R*)-MA from aqueous solution in the presence of (*S*)-MA were conducted in a seeded batch crystallizer. Final crystals with an *ee* of (*R*)-MA higher than 96.4% were obtained. On the basis of the records of the liquid concentration, nucleation and growth parameters were determined by tuning the model predicted concentrations to the experimental data using NSGA-II-JG. Solubility of the solution increases significantly compared to the equilibrium concentration of pure (*R*)-MA at the same temperature due to the presence of (*S*)-MA. This leads to the variation of supersaturation. Kinetic study confirmed the strong inhibition of the growth of the desired enantiomer in the presence of the opposite enantiomer for the seeded cooling crystallization resolution process. Such an inhibition effect becomes more significant with increasing concentration of the opposite enantiomer in the crystallization medium. In addition, the presence of (*S*)-MA was not observed to change the morphology and crystal habit of the final products.

Acknowledgment. This work presented was supported by Natural Sciences and Engineering Research Council, Canada, under Grant STGGP350490-07. All the calculations were performed using the facilities provided by Shared Hierarchical Academic Research Computing Network (SHARCNET: www.sharcnet.ca).

References

- (1) Subramanian, G. *Chiral Separation Techniques—A Practical Approach*; Wiley-VCH: Weinheim, 2001.
- (2) Jacques, J.; Collet, A.; Wilen, S. H. *Enantiomers, Racemates and Resolution*; Wiley: New York, 1981.
- (3) Lorenz, H.; Sheehan, P.; Seidel-Morgenstern, A. *J. Chromatogr., A* **2001**, *908*, 201–214.
- (4) Strohlein, G.; Schulte, M.; Strube, J. *Sep. Sci. Technol.* **2003**, *38*, 3353–3383.
- (5) Randolph, A. D.; Larson, M. A. *Theory of Particulate Processes*, 2nd ed.; Academic Press: New York, 1988.
- (6) Nagy, Z. K.; Fujiwara, M.; Woo, X. Y.; Braatz, R. D. *Ind. Eng. Chem. Res.* **2008**, *47*, 1245–1252.
- (7) Trifkovic, M.; Sheikhzadeh, M.; Rohani, S. *Ind. Eng. Chem. Res.* **2008**, *47*, 1586–1595.
- (8) Profir, V. M.; Rasmuson, K. C. *Cryst. Growth Des.* **2009**, *9*, 315–323.
- (9) Perlberg, A.; Lorenz, H.; Seidel-Morgenstern, A. *Ind. Eng. Chem. Res.* **2005**, *44*, 1012–1020.
- (10) Lorenz, H.; Perlberg, A.; Sapoudjiev, D.; Elsner, M. P.; Seidel-Morgenstern, A. *Chem. Eng. Process* **2006**, *45*, 863–873.
- (11) Angelov, I.; Raisch, J.; Elsner, M. P.; Seidel-Morgenstern, A. *Chem. Eng. Sci.* **2008**, *63*, 1282–1292.
- (12) Lorenz, H.; Sapoudjiev, D.; Seidel-Morgenstern, A. *J. Chem. Eng. Data* **2002**, *47*, 1280–1284.
- (13) Lorenz, H.; Seidel-Morgenstern, A. *Thermochim. Acta* **2004**, *415*, 55–61.
- (14) Kaspereit, M.; Gedicke, K.; Zahn, V.; Mahoney, A. W.; Seidel-Morgenstern, A. *J. Chromatogr., A* **2005**, *1092*, 43–54.
- (15) Mughul, R. K.; Davey, R. J.; Black, S. N. *Cryst. Growth Des.* **2007**, *7*, 225–228.
- (16) Hu, Q.; Rohani, S.; Jutan, A. *Comput. Chem. Eng.* **2005**, 911–918.
- (17) Borissova, A.; Jammoal, Y.; Javed, K. H.; Lai, X.; Mahmud, T.; Penchev, R.; Roberts, K. J.; Wood, W. *Cryst. Growth Des.* **2005**, *5*, 845–854.
- (18) Cornel, J.; Lindenberg, C.; Mazzotti, M. *Cryst. Growth Des.* **2009**, *9*, 243–252.
- (19) Kim, K. J.; Mersmann, A. *Chem. Eng. Sci.* **2001**, *56*, 2315–2324.
- (20) Deb, K. *Multi-Objective Optimization using Evolutionary Algorithms*; John Wiley & Sons: Weinheim, 2001.
- (21) Zhang, Y.; Hidajat, K.; Ray, A. K. *Biochem. Eng. J.* **2004**, *21*, 111–121.
- (22) Agrawal, N.; Rangaiah, G. P.; Ray, A. K.; Gupta, S. K. *Ind. Eng. Chem. Res.* **2006**, *45*, 3182–3199.
- (23) Kasat, R. B.; Gupta, S. K. *Comput. Chem. Eng.* **2003**, *27*, 1785–1800.
- (24) Lewiner, F.; J. P. Klein, J. P.; Puel, F.; Févotte, G. *Chem. Eng. Sci.* **2001**, *56*, 2069–2084.
- (25) Profir, V. M.; Furusjö, E.; Danielsson, L.; Rasmuson, Å. C. *Cryst. Growth Des.* **2002**, *2*, 273–279.
- (26) Mullin, J. W. *Crystallization*, 3rd ed.; Butterworth-Heinemann: Oxford, 1993.
- (27) Tung, H.-H.; Paul, E. L.; Midler, M.; McCauley, J. A. *Crystallization of Organic Compounds—An Industrial Perspective*; Wiley: Hoboken, 2009.
- (28) Garside, J.; Mersmann, A.; Nyvlt, J. *Measurement of Crystal Growth and Nucleation Rate*; IChemE: Rugby, 2002.
- (29) Mughal, R. K.; Davey, R. J.; Blagden, N. *Cryst. Growth Des.* **2007**, *7*, 218–224.
- (30) Patil, A. O.; Pennington, W. T.; Paul, I. C.; Curtia, D. Y.; Dykstra, C. E. *J. Am. Chem. Soc.* **1987**, *109*, 1529–1535.